Experimental and numerical study of the effects of ullage height on plume flow and combustion characteristics of pool fires

Liu, Chunxiang; Jangi, Mehdi; Ji, Jie; Yu, Longxing; Ding, Long

DOI:
10.1016/j.psep.2021.04.040

Document Version
Peer reviewed version

Citation for published version (Harvard):
Liu, C, Jangi, M, Ji, J, Yu, L & Ding, L 2021, 'Experimental and numerical study of the effects of ullage height on plume flow and combustion characteristics of pool fires', *Transactions of the Institution of Chemical Engineers, Part B - Process Safety and Env. Protection*, vol. 151, pp. 208-221. https://doi.org/10.1016/j.psep.2021.04.040

Experimental and numerical study of the effects of ullage height on plume flow and combustion characteristics of pool fires

Chunxiang Liu [a, b], Mehdi Jangi [b, *], Jie Ji [a, *], Longxing Yu [a], Long Ding [a]

[a] *State Key Laboratory of Fire Science, University of Science and Technology of China, Jinzhai Road 96, Hefei, Anhui 230026, China*

[b] *School of Mechanical Engineering, University of Birmingham, Edgbaston, Birmingham B15 2TT, UK*

Corresponding Author: Mehdi Jangi (M.Jangi@bham.ac.uk), Jie Ji (jijie232@ustc.edu.cn)

Abstract

Pool fires are frequently reported to trigger domino effects in oil storage farms and chemical factories. Fire plume is the vehicle of damage caused by pool fires. This study aims to study the effects of ullage height (distance between the fuel surface and the upper pool rim) on fire plume flow and combustion characteristics were conducted by experimental and numerical studies. Ullage heights were systematically changed from zero to the value at which the flame is self-extinguished. Simulations were validated against both time-averaged and instantaneous experimental measurements. In terms of the dynamic of the flame base with respect to the pool outlet, three classes were identified as follows. *Class I:* Flame base anchored near the upper pool rim, and the combustion was mainly of classic non-premixed flame type; *Class II:* Flame base entered into the pool but not merged; *Class III:* Flame base entered into the pool and merged along the middle axis. It was shown that the decreasing pressure near the pool outlet driven the flame to enter into the pool, as ullage height increased. According to the time-history of plume flow, three plume flow patterns were revealed at different ullage height conditions, which explained the evolutions of flame structures. It was shown that the percentage of premixing combustion was increased with ullage height. This behavior was attributed to the enhanced fresh air entrainment and mixing at the flame base.

Key Words: LES, plume flow, combustion mode, ullage height, flame characteristics, pool fire

Nomenclature	
h	Ullage height (m)
h^*	Nondimensional ullage height

D	Pool diameter (m)
m'	Mass loss rate (g/s)
$\bar{\rho}$	Filtered density (kg/m^3)
$\tilde{u}$	Favre-filtered velocity (m/s)
$\bar{\tau}_{ij}$	Filtered stress tensor (N/m^2)
$\tilde{Y}_a$	Favre-filtered mass species concentration (%)
$\tilde{h}$	Favre-filtered mass species enthalpy (J)
D_a	Material diffusivity (m^2/s)
D_F	Fuel diffusivity (m^2/s)
q^r	Radiative heat flux (J/s)
τ_{mix}	Characteristic mixing time (s)
τ_{chem}	Chemical time scale (s)
s_L	Flame spread length (m)
τ_d	Molecular diffusion time scale (s)
τ_u	Turbulent advection mixing time scale (s)
τ_g	Buoyant acceleration mixing time scale (s)
τ_{flame}	Acceleration controlled mixing time scale (s)
ε_{TC}	Emissivity of the thermocouple
δ	Stephan-Boltzmann constant, 5.67×10^{-8}/(m$^2\times$K^4)
U	Integrated radiative intensity (kW)
$h_{cond.}$	Conductive heat transfer coefficient (W/(m·K))
$h_{conv.}$	Convective heat transfer coefficient (W/(m·K))
T_g	True gas temperature (K)

T_{TC}	Temperature dumped from the simulation (K)
T_w	Temperatures of the pool sidewall (K)
C	Empirical coefficient
k	Gas thermal conductivity (W/(m·K))
Nu	Nusselt number
ρ_s	Solid density (kg/m^3)
ε	Emissivity of the gas
D^*	Characteristic diameter of the fire source
ρ_∞	Air density (kg/m^3)
T_∞	Air temperature (K)
c_p	Air specific heat (kJ/(kg·K))
g	Gravity acceleration (m/s^2)
$\dot{Q}$	Heat release rate (kW)
$R_{A,B}$	Correlation coefficient
Z	Mixture fraction
Z_{st}	Stoichiometric mixture fraction
$\nabla\rho$	Density gradient (kg/m^3/m)
∇P	Static pressure gradient (Pa/m)
Abbreviation	
SGS	Sub-grid Scale
HRR	Heat Release Rate
NIST	National Institute Of Standards And Technology
FDS	Fire Dynamics Simulator
LES	Large Eddy Simulation
FVM	Finite Volume Method
RTE	Radiation Transport Equation

FFT	Faster Fourier Transform
RMS	Root Mean Square

1. Introduction

Pool fire is one of the most frequently happened disasters in chemical productions and oil storage farms [1-5]. When an oil storage tank caught fire, due to the intense thermal hazards, the tank wall would subsequently fail and ultimately amplify the scale and consequence/damage of fire accidents along with the fuel leakage and spreading. This process is called as domino effects, if not well prevented or addressed, will cause severe consequences. Revealing the development and physical mechanism of pool fires has both fundamental and practical applications in process safety and risk analysis.

The classic definition of pool fire is "happening on the horizontal surface, buoyancy-driven diffusion combustion [6-7]". Studies about pool fires are mainly conducted in open space under near-zero ullage height (distance between fuel surface and the container/pool upper rim) conditions. These studies were mainly focused on the burning rate [8-12], flame height and pulsation [13-16], air entrainment [17, 18], flame radiation [19-22], and heat feedback [23, 24]. Revealing the effects of ullage height on the burning behaviors of pool fires, yet has to be done. This is motivated by the fact that, in a real fire, ullage height often increases as the fire progresses, which can significantly change the nature of pool fires and the associated parameters. For example, when a fuel tank caught fire, the mass loss rate changed notably as the ullage height increased [25]. When applying the in-situ burning method to clear the fuel leakage on the ice, the cleaning efficiency was significantly affected by the ullage height [26, 27]. Besides, ullage height will also influence the garbage combustion process burned in an open pit [28]. It is anticipated that at nearly zero ullage height conditions (in open space), the fresh air freely enters to the fire zone, and mixes with the evaporated fuel. While under ullage height conditions, the processes of entrainment and mixing are substantially affected in such a way that is not very clear at the moment. Besides, the mechanism of heat transfer (conduction and radiation) from the ullage to the fuel can

also change and play an essential role in the overall characteristics of the fire. Relevant studies are as follows. Blinov and Khudyakov [8] investigated the flame characteristics of aviation fuel and isoamyl alcohol pool fires under different fuel level depth (ullage height) conditions. They pointed out that ullage height would change the mass loss rate and flame behaviors. Specifically, the flame behaves more turbulence and enters into the pool as ullage height increases to a certain extent. Ankit et al. [25] studied the maximum burning rate of tank fires with different experimental setups (with and without constant fuel supply). They found out that the mass burning rate increased by 30%-46% when the model tank was connected to a constant fuel supply device. Magnus [29] studied the effects of freeboard height (ullage height) on burning behaviors of ethanol and gasoline pool fires. He found that the maximum flame height and mass loss rate decrease with the increase of ullage height. Dlogugorski and Wilson [30] measured the mass loss rate of ethanol pool fires, and correlated an empirical model between mass loss rate m' and the non-dimensional ullage height h^* ($h^*=h/D$) as, $m' \propto \exp(-h^*)$. Hu et al. [31] analyzed the flame necking-in and instability characteristics of pool fires under minor ullage height conditions, ranging from 0.3 cm to 2 cm. They found that the depth and velocity of flame necking-in are sensitive to the change of ullage height. Shi et al. [32] studied the flame characteristics of methanol pool fires with the influence of ullage height. They observed that the flame presents a characteristic of partially premixed combustion under higher ullage height conditions. But they did not give any evidence to support their deduction. Kuang et al. [33] studied the evolution of mass loss rate under the effects of ullage height and crosswind, and fitted a model considering the ullage height and crosswind speed. Liu et al. [34] investigated the effects of ullage height on flame characteristics and proposed an equivalent hydraulic diameter to modify classic flame height and oscillation models. The influence of ullage height on plume centerline temperature was revealed by Liu et al. [35], with a new virtual origin model developed and a new plume centerline temperature model correlated. Concerning the effects of ullage height on heat transfer mechanisms, Ma et al. [36] numerically studied the influences of lip (ullage) height on the dynamics of methanol

pool fires. They reported that, due to the changed plume flow and flame base instability, the flame tended to be wider and shorter, which would change the heat feedback toward the fuel surface. However, only a very minor ullage height condition (h/D=0.03) was involved in their studies. How the flame characteristics and plume flow will evolve under varying ullage height conditions are still unknown.

To summarized, the above studies have found that ullage height has significant effects on the mass loss rate and flame behaviors of pool fires. But, there are still some important issues that need to be clarified as follows.

(1) It has been revealed that flame would enter into the pool when the ullage height increases to a certain extent [8, 30, 32]. However, the key underlying physical mechanism is still unknown. For example, it is not clear that what is the combustion mode and stabilization mechanism of the flame based as it enters inside the pool, and how they respond to the variation of the ullage height conditions.

(2) It has been found that the flame structure is notably changed under different ullage height conditions [8, 29, 31]. However, the fundamental dynamic characteristics of the fire plume at different ullage height are not fully understood.

Experiments are revealing but are not sufficient in answering all these questions. The reason is that the problem of pool fires at various ullage heights involves a multiscale physical process that interacts with each other in a very non-linear manner which cannot be fully resolved in physical experimentations. First of all, it is hard to observe the flame characteristics inside the pool. Even if we use a transparent quartz pool, the ullage will be blackened by the flame. Secondly, it is also not easy to apply flow field devices to characterize the flow field within the pool. Three-dimensional and unsteady numerical simulations provide a unique opportunity to observe these phenomena and reveal the underlying physical mechanisms. Here, we present a variety of own experiments with ullage height increased from 0 to the value that the flame self-extinguished. During each experiment, the flame structure, plume centerline temperature, and flame oscillation frequency were measured. This will follow by showing the simulation results which have been systematically validated based on both

time-averaged and the instantaneous results. Afterward, the evolutions of the flame characteristics, patterns of plume flow, and combustion modes and the stabilization mechanisms of the flame base under various ullage height are explored.

2. Experimental setup

Figure 1 shows the experimental setup. The experiments were conducted in a quiescent environment with an ambient temperature of 283 K. The local atmospheric pressure was 101 kPa. The experimental setup mainly consisted of three parts, including the combustion module, the dynamic fuel supply system, and the measurement devices. As shown in Fig. 1, the combustion module included a well transparent quartz pool where the combustion happens. The pool upper rim was lifted 1 m above the ground. A supporting platform was used to keep the quartz pool steady and safe. The inner diameter and inner height of the quartz pool were respectively 150 mm and 500 mm. A dynamic fuel supply system was designed and customized based on the communicating theory to dynamically supply n-heptane fuel to the combustion module.

As shown in Fig. 1, the fuel supply system mainly contains three tanks: the fuel supply tank, the fuel overflow tank, and the fuel reservoir tank. Valves 1~3 were kept on, and valve 4 was kept closed before each test. Experimental fuel flowed from the fuel supply tank into the fuel overflow tank then into the right pool. The fuel overflow tank was separated into two parts. During each test, the fuel level in the left part of the fuel overflow tank remained full and shared identic fuel level with that of the experimental pool. The excess fuel overflowed to the right part, then through valve 3 into the fuel reservoir tank. After each test, valves 1~3 were closed, and valve 4 was opened to recycle the pool's remaining fuel. After that, all the collecting fuel was pulled into the fuel supply tank from the two fuel reservoir tanks. The fuel supply volume was automatically adjusted based on the fuel consumption rate. Thus the ullage height (h) was always kept constant during each test. This method’s reliability is well recognized in the study of pool fires [25, 30, 31]. h was achieved by adjusting the height of the oil supply system through a precise electronic elevator. The uncertainty of the height

adjustment was less than 1 mm. Each test generally lasted around 3600 s to reach a steady burning stage. It should be noted that test results obtained from the experiments were intercepted form the steady burning stages (around 200 s). Through experiments, it had been found that the flame will self-extinguish when *h* was above 210 mm. The analyzed *h* included 0 mm, 15 mm, 30 mm, 45 mm, 60 mm, 75 mm, 90 mm, 105 mm, 120 mm, 135 mm, 150 mm, 180 mm, and 210 mm. The measurement devices included a K-type thermocouple tree placed on the pool's central axis, with a space interval of 5 cm between two adjacent thermocouples. The diameter of the thermocouple was 1 mm. And the response time was less than 1 s. This type of thermocouple was widely used in previous studies [8, 9, 16].

A digital HD camera with a spatial resolution of 1920 x 1080 and frame rates of 50 fps was used to record the flame structure. The obtained video was converted frame by frame. And those images recorded during the steady burning stage were used to validate the numerical model. Ostu method was applied to processing these images to obtain the statistical data of the flame characteristics, which was proved to be a reliable method [37-39]. An electronic balance with a precision of 0.1 g was adopted to record the fuel consumption rate.

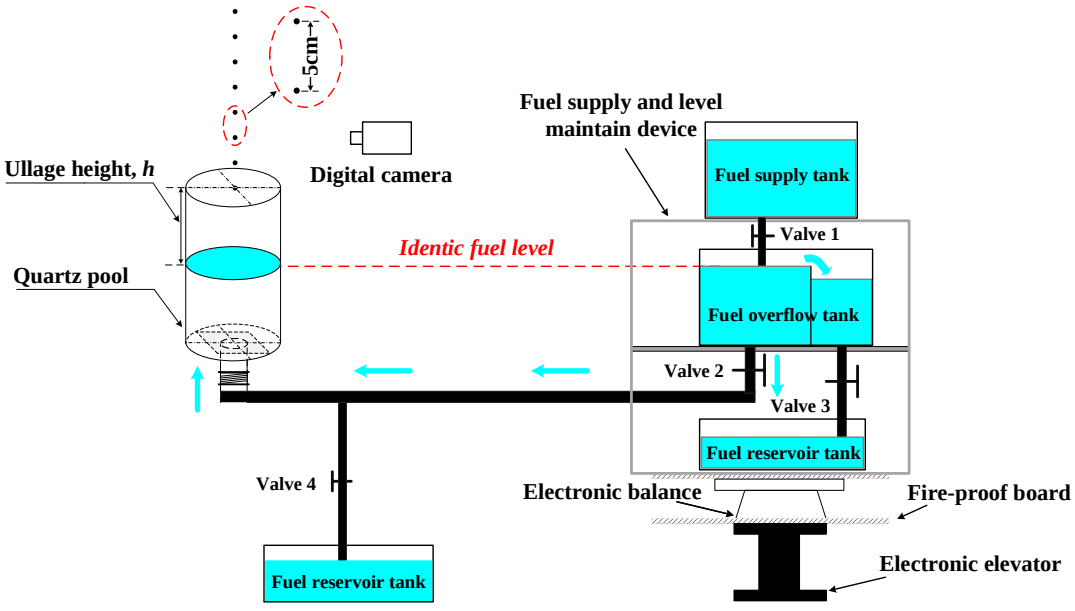

Fig. 1 Sketch diagram of experimental setup

The detailed physical properties of the fuel and the pool are listed in Table 1.

Table 1 Physical properties of quartz and n-heptane

Properties	**Quartz pool**	**n-Heptane**
Boiling point (℃)	\	98.5
Density (kg/m^3, 20℃)	2200	675
Heat of vaporization (kJ/kg)	\	317
Heat of combustion (MJ/kg)	\	44.6
Conductivity (W/m·K)	1.4	0.14
Specific heat (kJ/kg·K)	0.67	2240
Emissivity	0.775	1
Absorption coefficient (1/m)	40000	333

3. Mathematical model and numerical setting

In this study, a computational fluid dynamics-based software, Fire Dynamics Simulator (FDS), was used to simulate the fire plume under different ullage height conditions. FDS was developed by the National Institute of Standards and Technology (NIST), and is capable to simulate low-speed (Ma < 0.3), thermally-driven flow [40]. Previous studies have proved that FDS could accurately predict the qualitative and quantitative fire behaviors [41-44], by applying Large Eddy Simulation (LES).

3.1 The governing equations

Favre-filtering LES conservations are given as:

$$\frac{\partial \bar{\rho}}{\partial t}+\frac{\partial \bar{\rho}\tilde{u}_j}{\partial x_j}=0 \tag{1}$$

$$\frac{\partial \bar{\rho}\tilde{u}_i}{\partial t}+\frac{\partial \bar{\rho}\tilde{u}_i\tilde{u}_j}{\partial x_j}=-\frac{\partial \bar{P}}{\partial x_i}+\bar{\rho}g+f_i+\frac{\partial}{\partial x_j}(\overline{\tau_{ij}}-\tau_{ij}^{sgs}) \tag{2}$$

$$\frac{\partial (\bar{\rho}\tilde{Y}_a)}{\partial t}+\frac{\partial (\bar{\rho}\tilde{Y}_a\tilde{u}_j)}{\partial x_j}=\frac{\partial}{\partial x_j}(\overline{\rho D_a}\frac{\partial \widetilde{Y_a}}{\partial x_j}-\varphi_{Y_a}^{sgs})+\bar{\rho}\tilde{\dot{w}}_a \tag{3}$$

$$\frac{\partial (\bar{\rho}\tilde{h})}{\partial t}+\frac{\partial (\bar{\rho}\tilde{u}_j\tilde{h})}{\partial x_j}=\frac{D\bar{P}}{Dt}-\frac{\partial \left(q_j^r\right)}{\partial x_j}+\frac{\partial}{\partial x_j}(\bar{k}\frac{\partial \tilde{T}}{\partial x_j}-h_j^{sgs}) \tag{4}$$

where $\bar{\rho}$ is the filtered density, $\tilde{u}$ is the Favre-filtered velocity, $\bar{\tau}_{ij}$ is the filtered stress tensor obtained from the resolved strained rate. $\tilde{Y}_a$ and $\tilde{h}$ are the Favre-filtered mass species concentration and enthalpy, D_a is the mass diffusivity, q^r is the radiative heat flux, DP/Dt is the material derivative, $\tilde{\dot{w}}_a$ is the Favre-filtered species source term. The overline represents a Favre-filtering quantity [1]: $\tilde{\phi} = \overline{\rho\phi}/\bar{\rho}$. Terms τ_{ij}^{sgs}, $\varphi_{Y_a}^{sgs}$ and h_j^{sgs} require closure in order to close the set of Eqs. (1)-(4). The sub-grid stress τ_{ij}^{sgs} tensor is modeled using Smagorinsky model, $h_j^{sgs} = -\overline{\rho C_p}\frac{\upsilon^{sgs}}{Pr^{sgs}}\frac{\partial \tilde{T}}{\partial x_j}$ and $\varphi_{Y_a}^{sgs} = -\bar{\rho}\frac{\upsilon^{sgs}}{Sc^{sgs}}\frac{\partial \widetilde{Y_a}}{\partial x_j}$, where υ^{sgs}, Sc^{sgs} and Pr^{sgs} are the sub-grid eddy viscosity, Schmidt number and Prandtl number, respectively.

3.2 The combustion models

Here, we adopted the most commonly used combustion model, which is based on the mixing-controlled infinite fast chemistry model. In the current study, a turbulent batch reactor model is applied to handle the turbulence-chemistry interaction in the partially premixed combustion mode [40]. The basic idea of this model is that it treats each computational cell as a turbulent batch reactor, among which the concentration of each specie and mixing degree is computed. The converting rate of reactants to products is determined by a characteristic mixing time, τ_{mix}. Based on the local state of the flow field, an expression for τ_{mix} is incorporated in FDS as follows [45],

$$\tau_{mix} = \max(\tau_{chem}, \min(\tau_d, \tau_u, \tau_g, \tau_{flame})) \tag{5}$$

where τ_{chem} represents chemical time scale, $\tau_{chem} \sim D_F/(s_L)^2$, D_F is the diffusivity of the fuel, s_L is the flame spread. $\tau_d = S_{C_t}\bar{\rho}\Delta^2/(\mu+\mu_t)$ is the molecular diffusion time scale. $\tau_u = \Delta/(\sqrt{2k_{sgs}})$ is the turbulent advection mixing time scale. τ_g is the buoyant acceleration mixing time scale. τ_{flame} is the acceleration controlled mixing time scale for highly turbulent flames. For the present studies presented later where the

grid spaces stay within a quarter of the minimum flame dimension, τ_{flame} is ignored as suggested [46]. Equation 5 incorporates the physical processes associated with the molecular diffusion, the sub-grid scale (SGS) advections, and the buoyant acceleration. The mixing time is then calculated as the fastest time scale.

3.3 The turbulence model

In FDS, SGS flux terms are closed by the turbulence model. Specifically, two turbulent transport coefficients, namely turbulent viscosity, and the turbulent diffusivity are respectively used to close the SGS momentum and the scalar flux terms. Turbulent diffusivity is calculated using constant Schmidt number and Prandtl number [45] (0.5 for both). The turbulent viscosity μ_t in this study is obtained based on Deardorff model [45], which has been validated or compared by a wide of experiments. Deardorff model is given as [45]:

$$\mu_t = \rho C_v \Delta \sqrt{k_{sgs}} \tag{6}$$

3.4 Computational domain and boundary conditions

Figure 2 shows the computation domain and boundary conditions. The detailed geometric setup and grid cell size are discussed in Section 4.1. Open boundary conditions are set at the sides and the top of the computational domain. Gases (surrounding air and combustion products) may freely enter and leave the computational domain through the open boundaries. Simple upwind boundary condition is applied near the computational domain. Exterior values of temperature, pressure, mass fractions and other physical parameters are respective taken for the incoming flow. While for the outgoing flow, respective values in the grid cell adjacent to the boundary are taken. Usually, it is easier to set a rectangular pool through FDS. This, however, doesn't match the cylindrical shape of the pool in the experiments. To address this problem, the cylindrical wall of the pool was approximated by a fine series of the Cartesian mesh as shown in Fig. 2. Thermocouples were placed along the plume

centerline as specified in the experiments. It should be noted that, in FDS, the temperature measured by the thermocouple is not the gas temperature and solved by the following equation [45].

$$\varepsilon_{TC}(\delta T_{TC}^4 - U/4) + h_{cond.}(T_{TC} - T_g) = 0 \tag{7}$$

where ε_{TC} is the emissivity of the thermocouple and equals 0.85, δ is the Stephan-Boltzmann constant, U is the integrated radiative intensity, $h_{cond.}$ is the conductive heat transfer coefficient, T_g is the true gas temperature, T_{TC} is the temperature dumped from the simulation. Effects of the flame radiation on the temperature field were considered in the simulation. Thus, the experimental temperature data were not needed to correct for the radiative error.

3.5 Conduction models

Near the wall, constant coefficient Smagorinsky (0.2) with Van Driest damping was used for the eddy viscosity in the first off-wall grid cell. The thermal boundary conditions of the wall were set as “exposed”, which means the convective and radiative heat transfer between the pool sidewall and the surrounding air were calculated. In the current LES calculation, the natural/forced convective heat flux near the wall boundary is obtained as [40],

$$\dot{q}_c'' = h_{conv.}(T_g - T_w),\ h = \max[C\left|T_g - T_w\right|^{1/3}, \frac{k}{L}Nu] \tag{8}$$

$$Nu = C_1 + C_2\,\mathrm{Re}^n\,\mathrm{Pr}^m \tag{9}$$

where $h_{conv.}$ is the convective heat transfer coefficient. T_g and T_w are the temperatures of the nearby gas and the pool sidewall. C is an empirical coefficient (1.52 for horizontal plate and 1.31 for a vertical plane or cylinder). L is a characteristic length related to the size of the physical obstruction. For planner surfaces, L equals to 1 m, while for cylindrical surfaces it equals to the cylinder diameter [45]. k is the gas thermal conductivity. Nu is the Nusselt number, which is influenced by the geometric and the

flow characteristics. The detailed values for C_1, C_2, n and m could be found in Ref. [45].

One-dimensional heat conduction equation was applied for calculating the solid phase (inside the pool sidewall) temperature T_s (x, t) profiles.

$$\rho_s c_s \frac{\partial T_s}{\partial t} = \frac{\partial}{\partial x}(k_s \frac{\partial T_s}{\partial x}) + \dot{q}_s''' \tag{10}$$

where ρ_s is the solid density, c_s is the specific heat of the solid material. T_s is the solid temperature at the solid surface when $x = 0$. x is the distance normal to the solid surface. $\dot{q}_s'''$ is the source term, consisting the chemical reactions and radiative absorption. As shown in Fig. 2, constant heat release rate boundary conditions were set at the burning surface, based on the experimental results. Boiling condition was assumed at the burning surface, i.e. the mass fraction of heptane equals to 1 and the temperature equals to the boiling temperature at 1 atm.

3.6 Radiation and soot

Similar equations as the Finite Volume Method (FVM) was applied to solve the radiation equation. Approximate 100 discrete angles are updated over multiple time steps. Soot is considered the most important species that controls thermal radiation from fire plume. Thermal radiation in the energy equation is defined by [45]:

$$\dot{q}_r''' = -\nabla \cdot \dot{q}''(x) = \kappa(x)[U(x) - 4\pi I_b(x)] \tag{11}$$

$$U(x) = \int_{4\pi} I(x, s')ds' \tag{12}$$

where $I_b(x)$ is the source term, and $I(x, s')$ is the solution of the radiation transport equation (RTE). $\kappa(x)$ is the absorption coefficient, calculated by a narrow-band model called RadCal [47].

The radiative heat transfer near the wall boundary is calculated based on the assumption that the thermal radiation from the surrounding gases is absorbed within an infinitely thin layer at the surface of the wall. The incoming and outgoing radiative heat flux of the wall are obtained as [45],

$$\dot{q}''_{r,in} = \varepsilon \int_{s'\cdot n_w<0} I_w(s')\left|s'\cdot n_w\right| d\Omega \tag{13}$$

$$\dot{q}''_{r,out} = \varepsilon\sigma T_w^{\ 4} \tag{14}$$

where ε is gas emissivity, I is the radiation intensity per unit of solid angle, s is the unit vector in direction of radiation intensity. n_w is the partial reaction order for the wall. Ω is the solid angle. σ is the Stefan-Boltzmann constant.

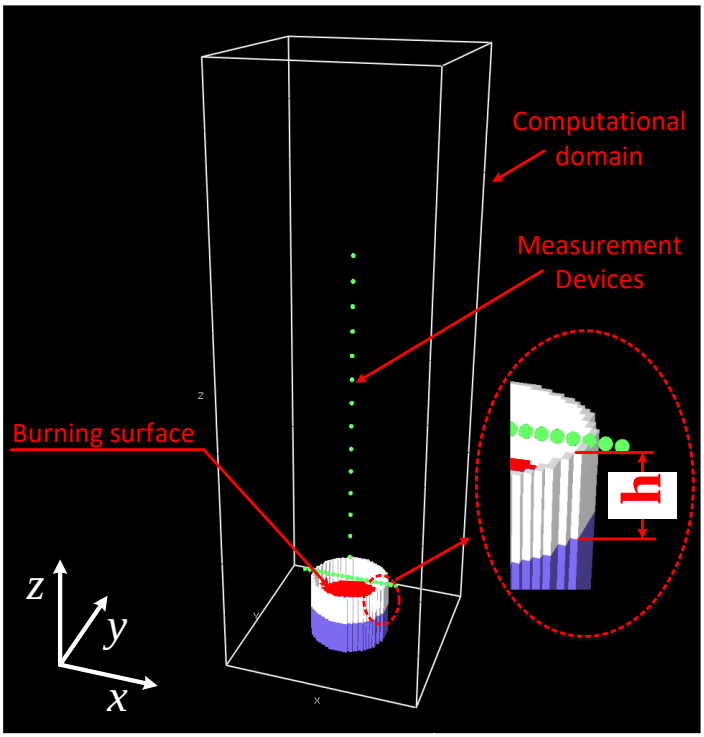

Fig. 2 Numerical setup

4. Results and discussion

4.1 Mesh sensitivity analysis and model validation

Extending computational domain size in x-, y-, and z-direction is required in order to properly resolve the flow field near the pool. Results are presented here are based on a computational domain with a height of 1.2 m in z-direction. Further extension of the domain in z-direction proven ineffective on the simulation results. Similarly, we examined various domain sizes in x- and y-direction as follows: 0.2 m x 0.2 m x 1.2 m, 0.4 m x 0.4 m x 1.2 m, and 0.8 m x 0.8 m x 1.2 m. In all cases, the computational domain was discretized into fully Cartesian grids which were refined toward the pool.

Several grids resolutions were examined to achieve grids independent results. D^*/δ_{cell} is the plume resolution index, D^* is the characteristic fire diameter, and is defined as,

$$D^* = \left(\frac{\dot{Q}}{\rho_\infty c_p T_\infty \sqrt{g}} \right)^{2/5} \tag{15}$$

where ρ_∞, T_∞ and c_p are respectively the density, temperature, and the specific heat of air. g is the gravity acceleration. $\dot{Q}$ is the heat release rate of the fire source, and is calculated according to experimental results. δ_{cell} is the nominal size of the grid cell. In the current study, the uniform grid cell is applied, because it has been proved that non-uniform ones will not necessarily improve the simulation accuracy but impair the computational efficiency [40]. Thus, all grid cells are set as uniform with $\delta = \delta_x = \delta_y = \delta_z$. It is recommended that the ideal plume resolution index is between 5 and 20 [48], depending on the specific scenarios. According to experimental results and Eq. 15, the recommended cell size is about 4.4 - 34.8 mm.

To determine a proper computation domain and grid cell size, the correlation coefficient is used to evaluate their influences on the accuracy of numerical model results. Experimental and simulated plume centerline temperatures are used to calculate the correlation coefficient. The mathematical equation is given as,

$$R_{A,B} = \frac{\Sigma(A-\bar{A})(B-\bar{B})}{\sqrt{\Sigma(A-\bar{A})^2 (B-\bar{B})^2}} \tag{16}$$

where A and B represent the analytic variables, here they are the simulated and experimental plume centerline temperatures. $\bar{A}$ and $\bar{B}$ are the corresponding averaged values. According to experimental results, when the ullage height *h* equals zero, the combustion intensity (mass loss rate) and the flame height achieve their highest values. Because the plume entrainment is positively correlated to the above two parameters, and they both decrease with ullage height. Zero ullage height condition, which is much more challenging than other non-zero ullage height conditions, is used to determine the proper computational domain and the grid cell size.

Figure 3 shows the correlation coefficient between experimental and simulated plume centerline temperatures, under different computational domains and grid cell sizes. Figure 3 demonstrates that generally the correlation coefficient increases with the computation domain and the plume resolution index. For the computation domain, the improvement between 0.2 m x 0.2 m x 1.2 m and 0.4 m x 0.4 m x 1.2 m is evident, under all sizes of the grid cell. However, as it is increased to 0.8 m x 0.8 m x 1.2 m from 0.4 m x 0.4 m x 1.2 m, the correlation coefficient remains almost constant. Then, it can be concluded that the computation domain of 0.4 m x 0.4 m x 1.2 m is sufficient to resolve the entrainment near the pool. Figure 3 also shows the effects of grids resolutions. It can be seen that for a given domain size, the correlation coefficient increases with the decrease of the cell size from 40 mm to 5 mm. However, further decreasing of the cell size to 4 mm, marginally changes the results. Thus, the cell size of 5 mm is used in all calculations. Figure 4 provides a comparison of the experimental and simulated plume centerline temperature profiles for zero ullage height conditions. While significant discrepancy between the simulated and experimental results is observed with a cell size of 40 mm, 20 mm, and 10 mm, the results with cell sizes of 5 mm and 4 mm are converged toward the experiments.

Besides, as shown in Fig. 5, typical non-zero ullage height conditions (h/D = 0.2, 0.5, 1, 1.4) are also provided to further verify the model reliability. As shown in Fig. 5, the numerical model generally reproduces the maximum and the profiles of the plume centerline temperature and proves that the adopted computation domain (0.4 m x 0.4 m x 1.2 m) and the grid cell size (δ = 5 mm) are adequate. It should also be noted that the grid cell size applied here satisfies the criterion of at least 10 grids (30 grids used here) within the characteristic fire diameters to well simulate the fire plume behaviors proposed in literature [49].

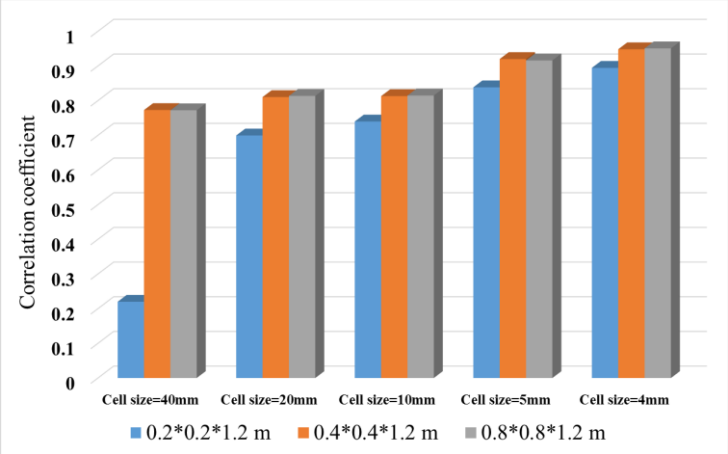

Fig. 3 Correlation coefficient of simulated and experimental results with different computation domains and grid cell sizes.

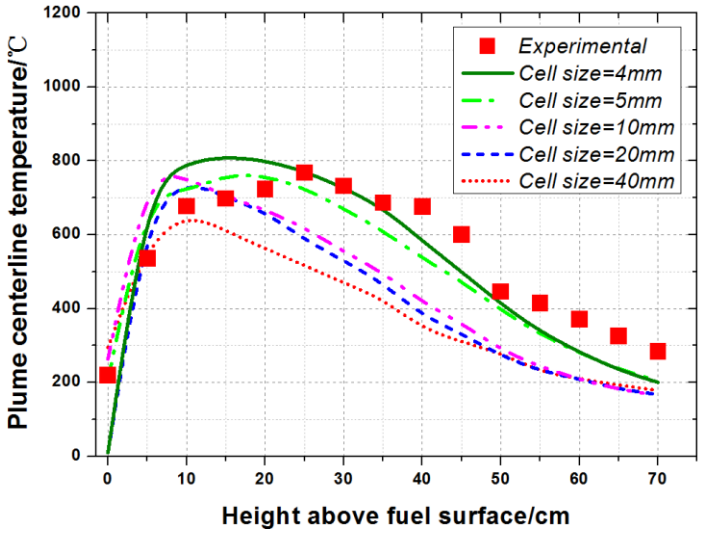

Fig. 4 Comparisons of simulated and experimental plume centerline temperature profiles.

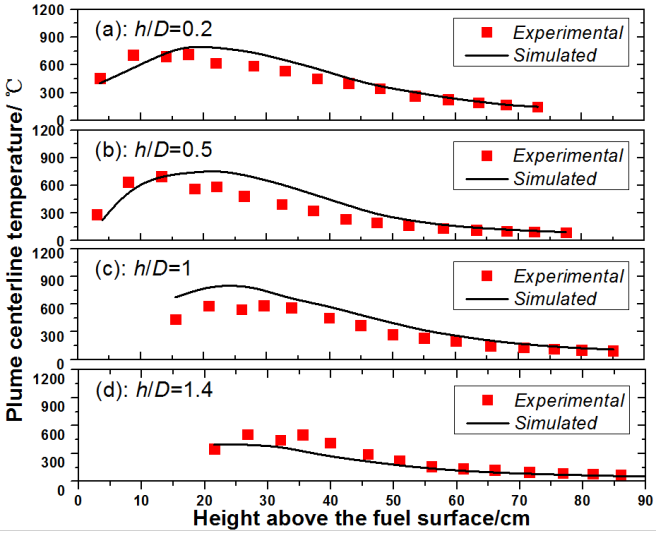

Fig. 5 Validation of the plume centerline temperature with h/D=0.25, 0.5, 1.0, 1.4.

Apart from using the above time-averaged data, the plume oscillation frequency is also used to validate the accuracy of the numerical model. This is important to the following plume flow discussions. The oscillation properties of the fire plume are the result of vortexes periodically forming and detaching from the plume boundary [50]. The experimental flame oscillation frequency is calculated by time-series (time-interval: 0.02 s) flame height data after Faster Fourier Transform (FFT). The simulated flame oscillation frequency is obtained by the time-series vertical velocity (W-velocity) after FFT. This method has been verified by previous works [51-54]. Figure 6 gives the typical power spectrum of the simulated plume vertical velocity averaged from four time-series locations. Two velocity detectors were placed along the plume centerline in the plume intermittent zone with a space interval of 5 cm. Another two were placed around the plume boundary, sharing the same heights as the two placed along the plume axis. Figure 7 shows the comparison of simulated and experimental flame oscillation frequencies of all ullage height conditions. It can be seen in Fig. 7 that the agreements between simulations and experiments are remarkable.

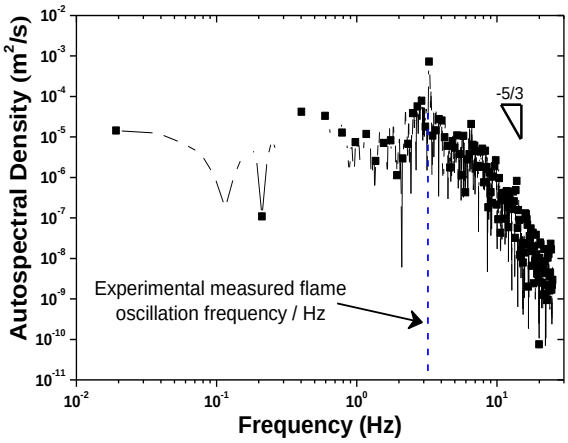

Fig. 6 Typical simulated power spectral densities of pool fires.

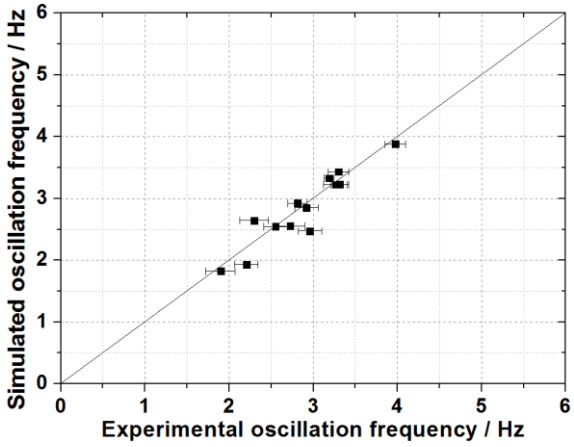

Fig. 7 Comparisons of the experimental and simulated plume oscillation frequency.

4.2 Flame characteristics and plume flow behaviors

Figure 8 gives the comparisons of the time-averaged distributions of experimental flame intermittency and simulated heat release rate of different ullage height conditions, intercepted over 10 s from the quasi-steady state period. Results in Fig. 8(a) are the experimental flame intermittency, shot from the plume front. The dark line donates that the flame intermittency (I) equals to 0.5 and 0.05, the height of which respectively represent the mean and maximum flame height [17]. The flame characteristics recorded during experiments are the results of the flame luminous which is essentially the glowing soot particles under high temperature [55]. Results in Fig. 8(b) are the cross-section of the time-averaged heat release rate (HRR), which indicates the region of high

combustion intensities. The black line represents the stoichiometric mixture fraction, Z_{st} (Z_{st} = 0.062, the detailed calculation is supplied in the Appendix). It should be noted that, different from Fig. 7(b), Fig. 8(a) is the projection of the front flame characteristics outside the pool. The front HD camera could not capture the flame characteristics inside the pool due to the shelter of the pool ullage sidewall.

From Fig. 8(a), it shows that both the mean and the maximum flame height decrease with h/D, due to the increasing air entrainment restriction effects by the pool ullage sidewall. Figure 8(b) shows that at h/D = 0, the flame manly anchors near the pool upper rim, without any significant HRR distributing in the interior region of the burning surface. The flame structure at this condition mimics the characteristics of non-premixed Bunsen flames. As ullage height increases, the fuel rich region (shown as the conical zone highlighted by the black dot line in Fig. 8(b)) gradually disappears, together with the flame base gradually entering into the pool. Especially, these cases can be categorized into three distinct categories. *Class I:* Flame base anchors near the pool upper rim, and the combustion is mainly of classic non-premixed flame type ($0 \leq h/D \leq 0.2$); *Class II:* Flame base enters into the pool but not merges ($0.2 < h/D \leq 0.9$); *Class III:* Flame base enters into the pool and merges along the pool axis ($h/D > 0.9$).

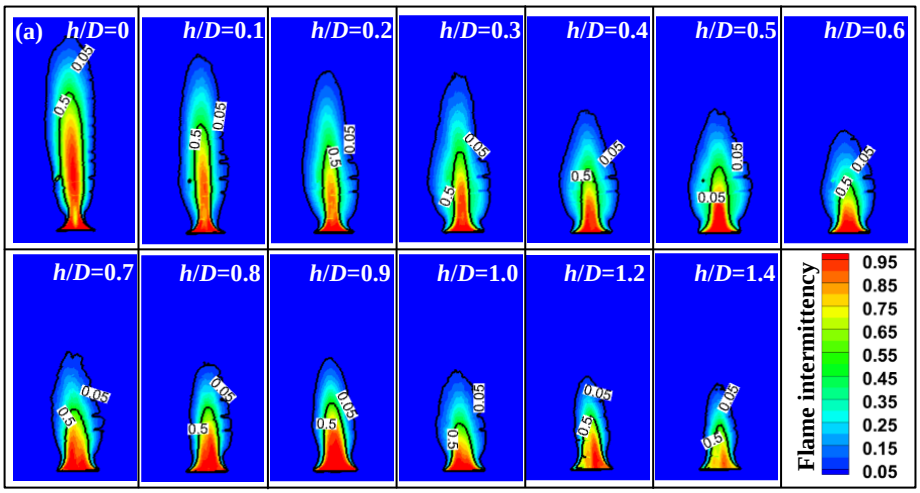

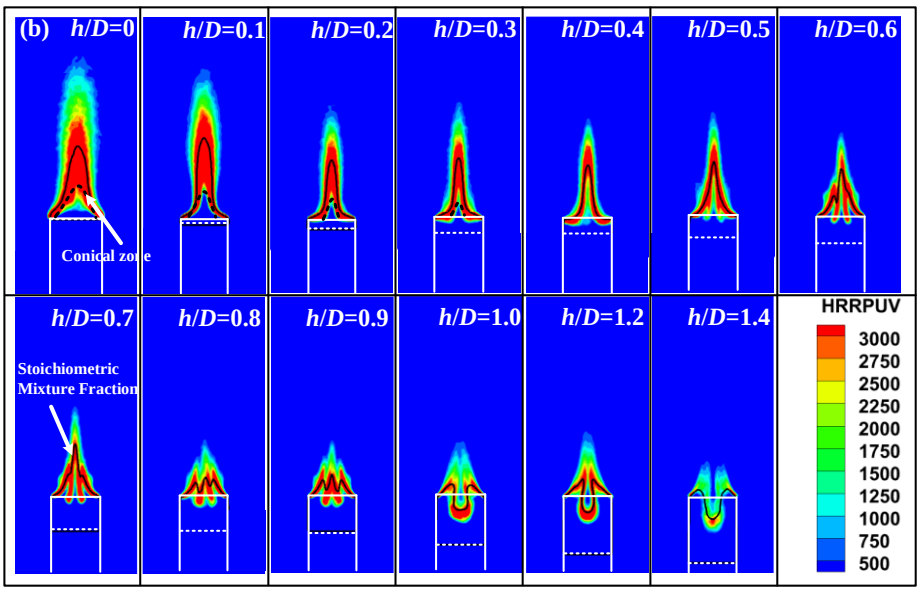

Fig. 8 Time-averaged distributions of experimental flame intermittency **(a)** and simulated heat release rate **(b)** under different ullage height conditions.

We now focus on the dynamics of the fire plume at various ullage heights. Figure 9 shows the time-history of the temperature distribution over the oscillation period of the flame height for different cases. As shown by the experimental snapshots in Fig 9(a), the *Class I* cases involve a rather stable conical zone and mimics the Bunsen type flame structure near the pool outlet, above which the flame tips oscillate with a certain frequency. Simulated results shown in Figs. 8(b) and 9(a) indicate a rather symmetric distribution of the HRR, temperature and velocity for this class of pool fires in the conical zone of the flame near the pool. This conical zone is caused by the buoyancy. Both experiments and simulations exhibit a laminar buoyancy-induced flow structure in this region. Instabilities are initiated at higher distance from the burning surface where the oscillating fire plume is formed. The plume vortexes asymmetrically distribute around the plume boundary. The generation of these vortexes is a result of the baroclinic vorticity generation mechanism [56]. Specifically, the misalignment of the static pressure gradient and density gradient leads to the twist of hot and cold fluid. Then, the twist fluid will develop into a rotational motion. This mechanism is expressed by the vector cross of two gradients as, $(\nabla\rho\times\nabla \mathrm{P})/\rho^2$ [57], where $\nabla\rho$ is density

gradient between hot plume gas and surrounding air in the horizontal direction, ∇P is the static pressure gradient under the influence of gravity in the vertical direction, and approximately a constant value, ρ is the plume density. Figure 10 shows the plume density and density gradient profiles of typical ullage height conditions in *Class I*. It demonstrates that ρ decreases first (in the conical zone) and then increases with the height. The decrease of the plume density in the conical structure attributes to the combustion process which continually heats the plume gas. Then, under the constant pressure condition, according to the ideal gas law, the plume density will decrease. After that, the increasing plume density results from high density cold air being entrained into the plume. While for the plume density gradient, a reverse trend is presented. And, the strongest vortex is formed in this turning point. Figure 9(b) gives the time-history of the distributions of temperature in *Class II*. According to the experimental snapshots, the conical structure disappears. The flame structure behaves like a periodically rising mushroom. Corresponding numerical results show that the ring vortex is formed inside the pool and around its upper rim. Outside the pool, the ring vortex develops and rolls upward, with its beneath flame being stretching thinner and thinner (t + 0.08 s ~ t + 0.24 s). Finally, the ring vortex detaches from the bulk flame (t + 0.32 s). The periodic initiation and development of the ring vortex well explain the flame puffing behaviors.

As shown in Fig. 9(c), in *Class III*, according to the experimental photos, the outside flame structure turns to be short and less turbulence. And, there seems a split in the flame center. Accordingly, the simulated results illustrate that, compared with *Class I & II*, there exists a “cold region” along the pool central axis, which means that the combustion there is not intense. And, different from *Class II*, the plume enters into the pool and merges there. Looking at the velocity streamline, it demonstrates that the plume outside the pool is relatively stable, with little vortexes formed and nearly straight streamline profiles. Inside the pool, the streamlines are very chaotic and several vortexes formed there. In *Class II & III*, surrounding air is entrained into the pool and mixed with fuel vapor there, causing the plume burning inside.

To reveal the physical mechanisms of why the plume could be entrained into the pool, and what makes it possible that the plume burns inside. Figure 11 gives the pressure and velocity-RMS (root mean square, RMS) profiles along the pool outlet of typical ullage height conditions of the three classes. Figure 11(a) reveals that the absolute value of negative pressure increases with ullage height, which explains why ambient air could be entrained into the pool. Distinct from *Class II & III*, axisymmetric peak negative pressure distributes near the pool outlet. The negative pressure zone is positively related to the buoyant acceleration process [58, 59]. As shown in Fig. 8(b), around the pool outlet, intense combustion (high HRR region) occurs around the pool upper rim in *Class I*. Then, buoyancy-induced acceleration would also be high there, which results in the peak negative pressure profiles. While for *Class II & III*, as shown in Fig. 8, the flame base enters into the pool. The differences of HRR distributions around the burner outlet is minor. Then, approximately equal buoyant acceleration will present there. As a result, the pressure profiles around the burner outlet are relatively flat.

As shown in Fig. 11(b), the velocity-RMS profiles characterize the plume turbulence properties and show an increasing trend from *Class I* to *Class III*. The increased plume turbulence will help to mix the entrained air with fuel vapor, which in the end makes it possible of plume burning inside the pool. Similarly, peak velocity-RMS around the pool outlet in *Class I* is a result of the combustion induced turbulence.

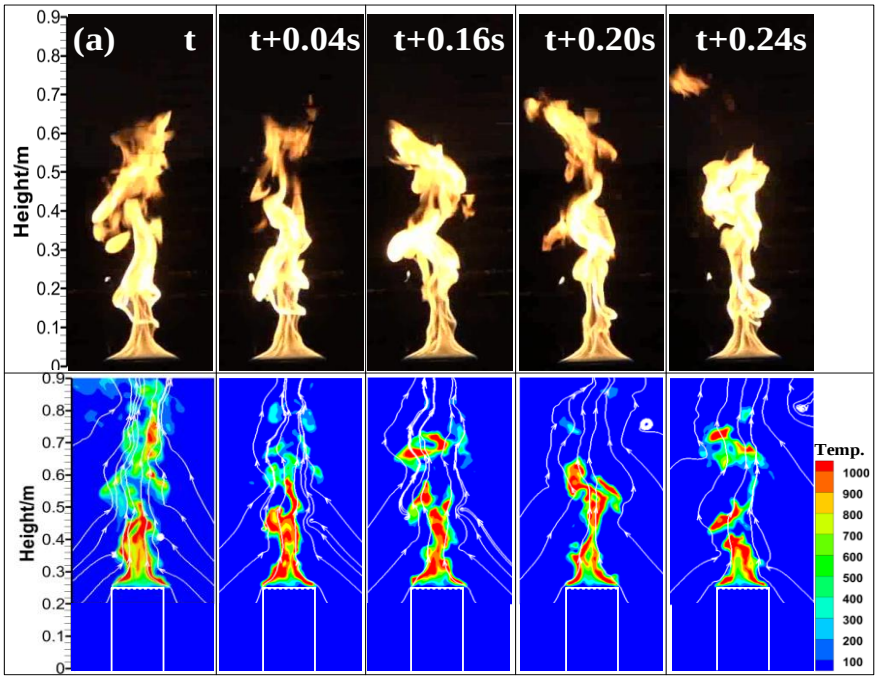
(a)
t
t+0.04s
t+0.16s
t+0.20s
t+0.24s
Height/m
Temp.
1000
900
800
700
600
500
400
300
200
100

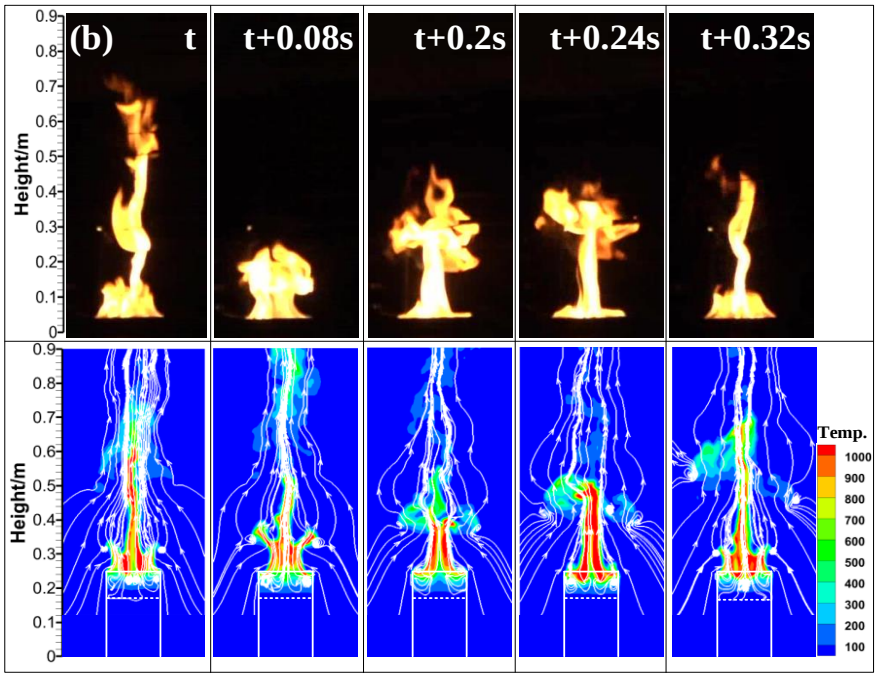
(b)
t
t+0.08s
t+0.2s
t+0.24s
t+0.32s
Height/m
Temp.
1000
900
800
700
600
500
400
300
200
100

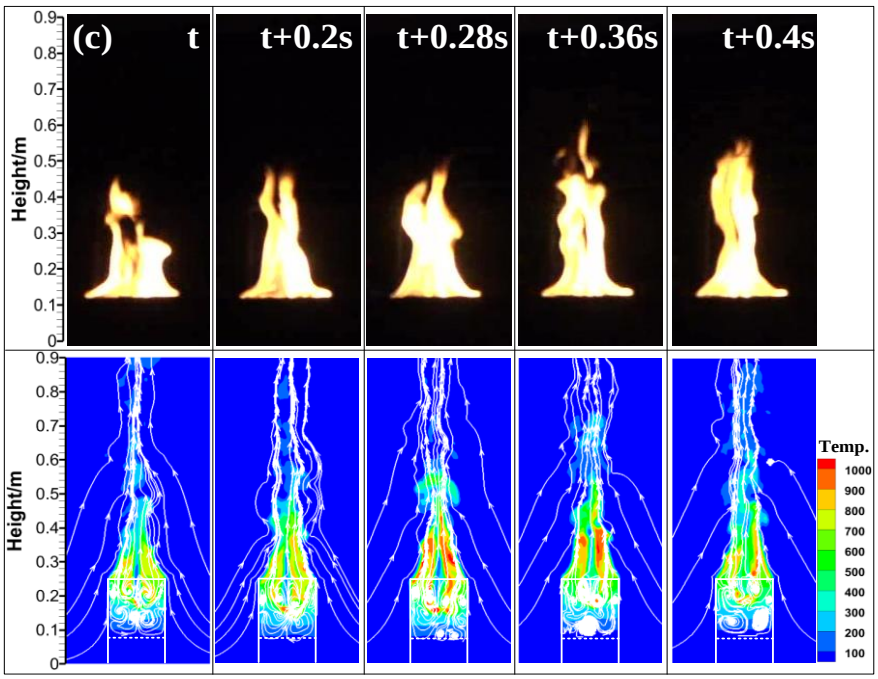

Fig. 9 Time-sequential experimental flame structure (outside the pool), simulated temperature and velocity streamlines: **(a)** *Class I*, **(b)** *Class II*, **(c)** *Class III.*

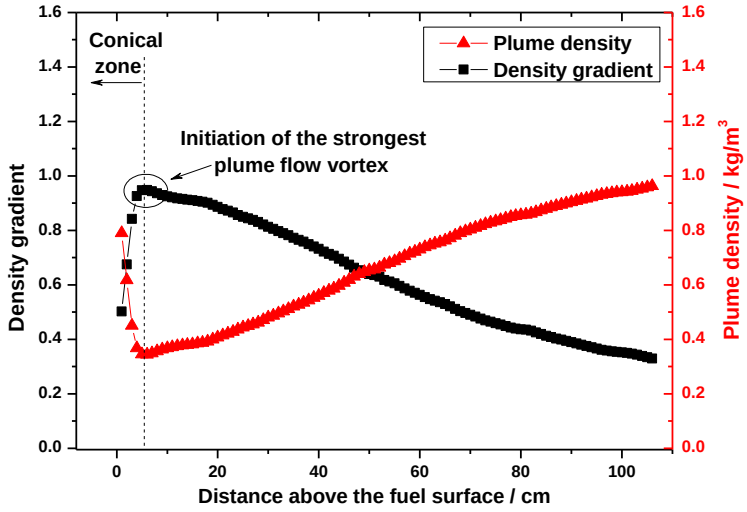

Fig. 10 Plume density and density gradient of *Class I*.

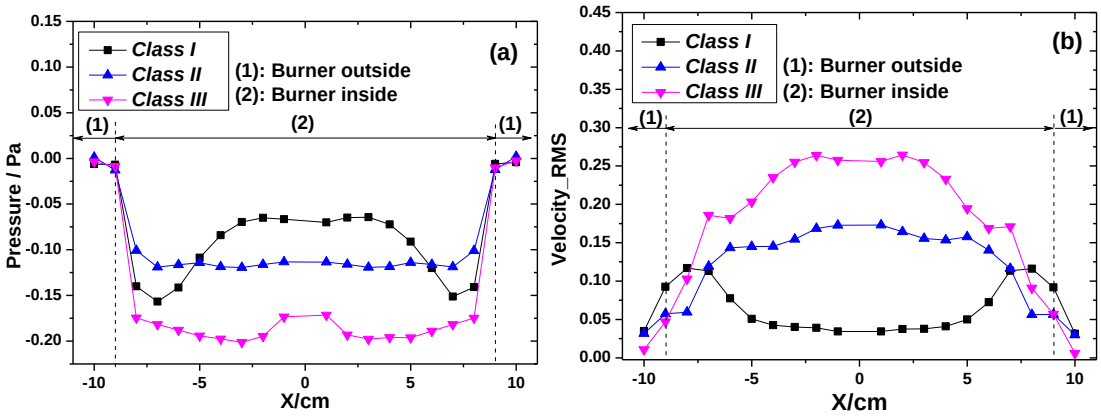

Fig. 11 Pressure and velocity-RMS profiles along the pool outlet:

(a) pressure, **(b)** velocity-RMS.

To better describe the processes of air entrained into the pool and plume gas leaving it, Figure 12 gives the time-history of the distributions of the plume velocity vectors within a flow cycle of *Class II* & *III*. In *Class II*, *a*s shown in Fig. 12 (a), ambient air entrained to the plume and enters into the pool under the effect of negative pressure (Fig. 11(a)). At the same time, ring vortexes centered on the pool axis are formed in the flow shear layer (t + 0.04 s). The vortexes continue to developing towards the axis (t + 0.04 s~ t + 0.08 s). After that, the ring vortexes carry and twist fuel vapor from the pool axis towards the pool rim and eventually flows outside (t + 0.08 s~ t + 0.16 s). Outside the pool, a large ring vortex is formed at the plume base, and passing downstream under the thermal buoyancy force (t + 0.16 s~ t + 0.24 s). While for *Class III* as shown in Fig. 11(b), the plume flow outside the pool is relatively stable and nearly does not change with time. Outside the pool, axisymmetric plume flow characteristic is demonstrated. Inside the pool, the plume flow is very chaotic, and generally the entrained air flows into the pool from part of its outlet and leaves it from another part. Based on the above analyses, the plume flow patterns of the aforementioned three classes are summarized in Fig. 13.

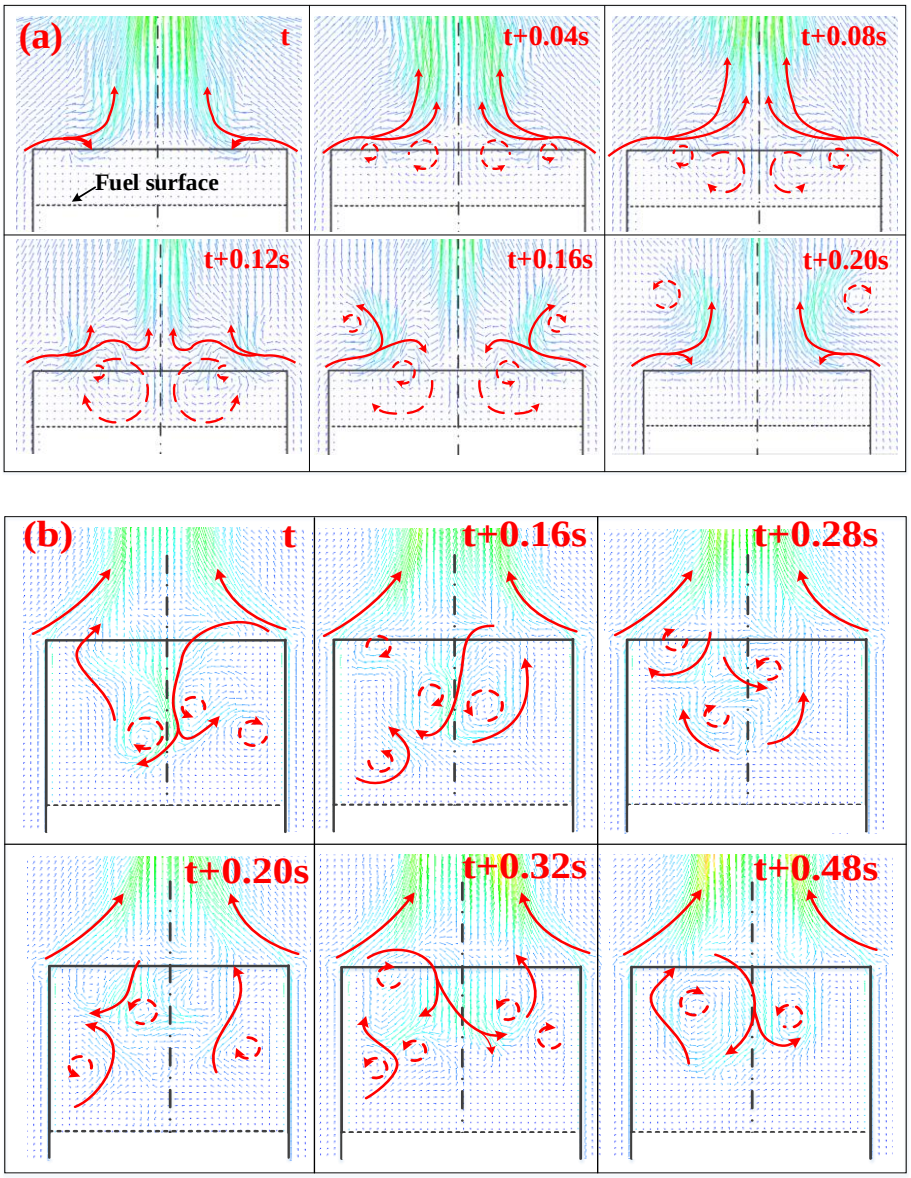

Fig. 12 Time-history of the distributions of velocity vectors within a flow cycle:

(a) *Class II*, **(b)** *Class III.*

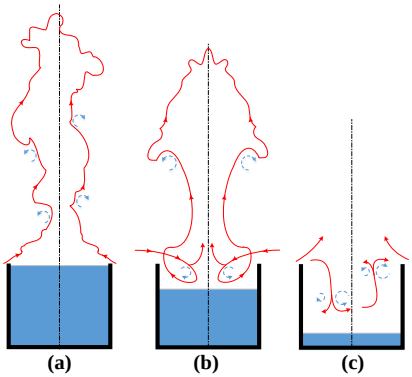

Fig. 13 Schematics of plume flow under different ullage height conditions:

(a) *Class I*, **(b)** *Class II*, **(c)** *Class III.*

4.3 Effects of ullage height on combustion modes

Figure 14 shows the time-history of HRR and oxygen fraction distributions. The white line represents the stoichiometric mixture fraction. The HRR distribution characterizes the location of the combustion reaction front (regions with high HRR). From Fig. 14, it demonstrates that the reaction front mainly distributes along the stoichiometric mixture fraction line. It is anticipated that if the combustion front occurs on the boundary of with and without oxygen, the combustion belongs to non-premixed combustion. Otherwise, the combustion will involve some levels of premixed combustion [60-64]. As shown by the oxygen fraction distribution in Fig. 14(a), the oxygen fraction inside the flame front (within the stoichiometric mixture fraction line) in *Class I* approximately equals to zero, and it slightly increases from *Class I* to *III.* This means that the percentage of premixed combustion increases with ullage height. The increased oxygen fraction inside the flame front attributes to the increased plume turbulence (indicated by the velocity-RMS shown in Fig. 11(b)) which enhances the stirring and mixing processes between the fuel vapor and the entrained air. Scatters of HRR as a function of mixture fraction is shown in Fig. 15 to further examine the combustion mode. In *Class I,* it can be seen that peak HRR mainly distributes in the fuel-rich zone (mixture fraction, $Z > 0.062$), which means the combustion is fuel-rich dominated and the mixing of fuel vapor and entrained air is limited before combustion. Then, non-premixed combustion mode is dominated. As ullage height increases, peak HRR shifts from the fuel-rich zone to the fuel-lean ($Z < 0.062$) zone, which confirms that the percentage of premixed combustion is increased.

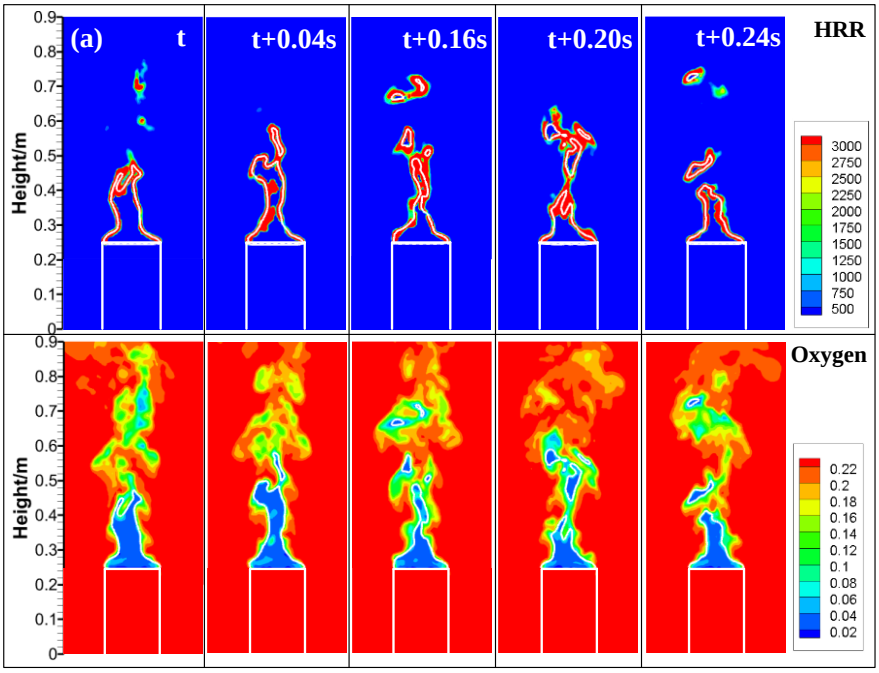
(a)
t
t+0.04s
t+0.16s
t+0.20s
t+0.24s
HRR
Oxygen
Height/m
0.9
0.8
0.7
0.6
0.5
0.4
0.3
0.2
0.1
0
3000
2750
2500
2250
2000
1750
1500
1250
1000
750
500
0.22
0.2
0.18
0.16
0.14
0.12
0.1
0.08
0.06
0.04
0.02

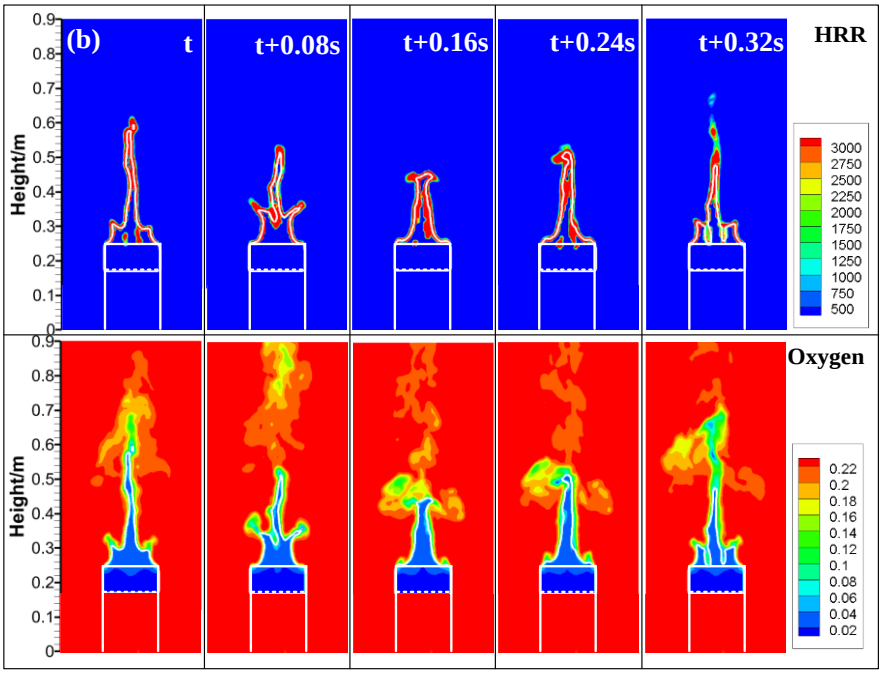
(b)
t
t+0.08s
t+0.16s
t+0.24s
t+0.32s
HRR
Oxygen
Height/m
0.9
0.8
0.7
0.6
0.5
0.4
0.3
0.2
0.1
0
3000
2750
2500
2250
2000
1750
1500
1250
1000
750
500
0.22
0.2
0.18
0.16
0.14
0.12
0.1
0.08
0.06
0.04
0.02

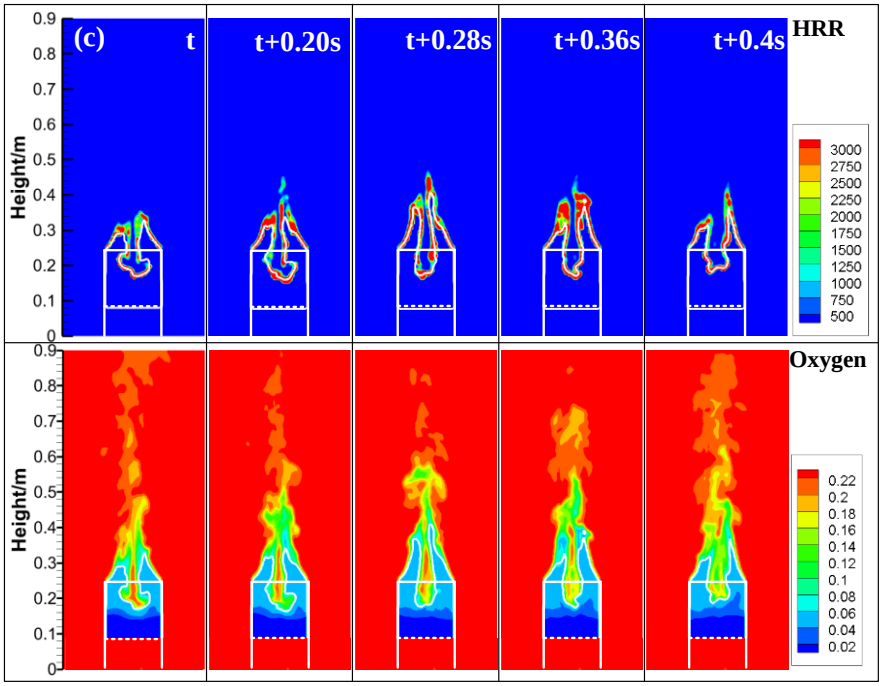

Fig. 14 Time-history of HRR and oxygen mass fraction distributions:

(a) *Class I*, **(b)** *Class II*, **(c)** ***Class** III.*

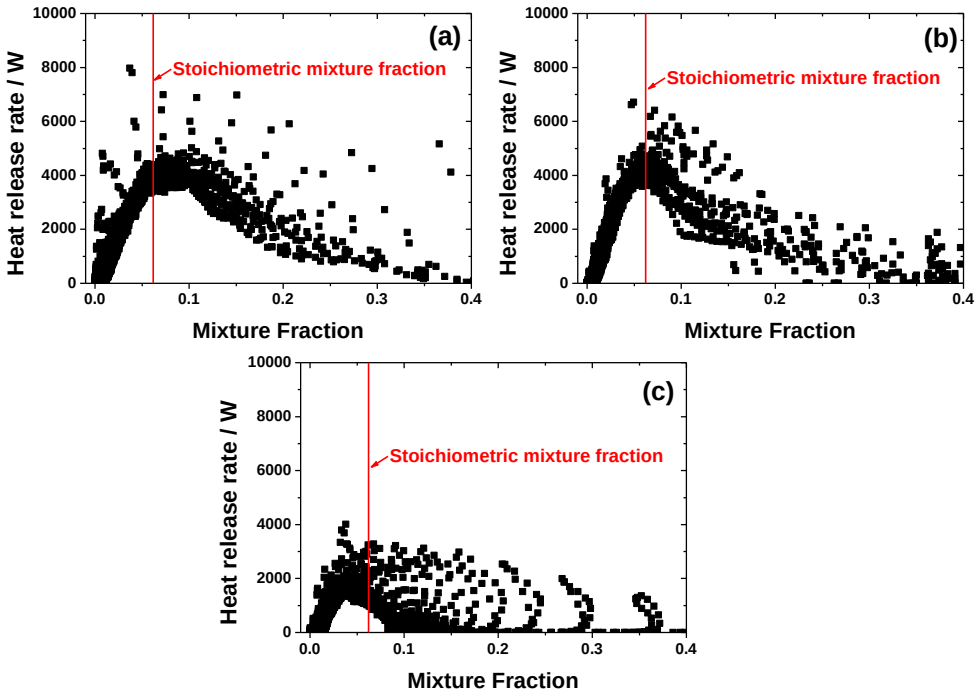

Fig. 15 HRR vs. mixture fraction: **(a)** *Class I*, **(b)** *Class II*, **(c)** *Class III.*

4.4 Discussion

This study analyzed the effects of ullage height on the fire plume flow and combustion characteristics of pool fires by the combinations of experiments and simulations. To model a burning tank fire from the beginning to the end, experiments were conducted with the ullage height systematically changed from zero to the value at which the flame self-extinguished. As ullage height increases, it was shown that, concerning the pool outlet, the fire plume base initially anchored around the pool outlet (*Class I*), then entered into the pool (*Class II & III*). When the fire enters into the tank, the strength of the tank wall might be soon weakened and eventually collapse. Thus, when dealing with the fire risk analyses of an oil storage farm, one needs to consider the thermal failure of the burning tanks and the following fuel leakage and flame spreading, especially when the tanks are far from fully-filled.

According to the experimental observations and the numerical results, it is anticipated that radiative heat transfer would be less dominant for significant ullage height conditions. During experiments, with the increase of ullage height, it was recorded that the fire plume became less luminous and produced less smoke. The weakening flame luminosity implies a decreased radiative temperature of the soot particles of the flame since the flame luminosity of the hydrocarbon fuels is mainly caused by the glowing soot particles [55]. And, soot usually plays the most critical role in flame radiation for hydrocarbon-fuels [64]. Then, it is reasonable to conclude that the flame radiative heat transfer would be less dominant as ullage height increases. According to the numerical results, the plume turbulence increases with the ullage height (Fig. 11(b)). For diffusion flame, the increased plume turbulence will reduce soot emission [65], which will lead to the decrease of radiative heat transfer.

The changed combustion mode shed light on the effects of ullage height on the combustion behaviors of pool fires. It is then anticipated that the flame emissivity and the heat transfer mechanisms from the fire plume would be different from those of zero or near zero ullage height conditions. To the authors' best knowledge, these remain unrevealed. Future work would then call for the detailed measurement of these parameters.

Conclusions

Experimental and numerical are combined to investigate the effects of ullage height (distance between the fuel surface and the upper pool rim) on pool fires' plume flow and combustion characteristics. Major findings are as follows.

(1). As ullage height increases, three classes could be classified based on the dynamic of the flame base concerning the pool outlet, namely, *Class I:* Flame base anchors near the upper pool rim, and the combustion is mainly of classic non-premixed flame type; *Class II:* Flame base enters into the pool but not merges; *Class III:* Flame base enters into the pool and merges along the pool axis.

(2). According to the time-history plume flow behaviors, three plume flow patterns under the effects of ullage height are revealed, and well explain the evolution of flame characteristics under the influence of ullage height.

(3). As ullage height increases, the combustion mode shifts from the classical non-premixed flame (zero ullage height) to partially premixed combustion (non-zero ullage height), resulting in the peak HRR region to shift from fuel-rich zone to fuel-lean zone.

This study's findings fundamentally revealed the effects of ullage height on flame characteristics, plume flow, and combustion modes of pool fires. And, these findings will benefit researchers or engineers, who are interested in the field of combustion, energy management and so on.

Appendix

In FDS, the combustion model is based on infinitely fast chemistry kinetics for a single step reaction,

$$a[\text{Fuel}] + b[\text{Oxidizer}] \longrightarrow \sum_{i=1}^{n} c_i[\text{Product}]_i \tag{A1}$$

The stoichiometric mixture fraction could be calculated as follows [45],

$$Z_{st} = \frac{m_{Oxidizer}}{m_{Fuel}c + m_{Oxidizer}},\ c = \frac{aM_{Oxidizer}}{bM_{Fuel}} \tag{A2}$$

where $m_{Oxidizer}$ and m_{Fuel} are the mass fraction of the oxidizer and fuel stream. $M_{Oxidizer}$ and M_{Fuel} are the molecular weight of the reacting oxidizer and fuel. For n-heptane, a=1, b=11, $m_{Oxidizer}$=0.233, m_{Fuel}=1, $M_{Oxidizer}$=32 g / mol, M_{Fuel}=100 g / mol. Then, input these values into Eq. (A2), the stoichiometric mixture fraction could be obtained as, Z_{st}=0.062.

Acknowledgements

This work was supported by National Natural Science Foundation of China (NSFC) under Grant No. 51722605, the Fundamental Research Funds for the Central Universities under Grant No. WK2320000038 and WK2320000040, and the National Post-doctoral Program for Innovative Talents (Grant No. BX20180288). Jie Ji was supported by the National Program for Support of Top-Notch Young Professionals and the Youth Innovation Promotion Association of CAS (2015386)

CRediT author statement

Chunxiang Liu: Investigation, Methodology, Writing - Original Draft, Formal analysis; **Mehdi Jangi**: Supervision, Writing - Review & Editing, Language polishing; **Jie Ji**: Conceptualization, Funding acquisition, Resources; **Longxing Yu**: Methodology, Formal analysis; **Long Ding**: Methodology, Formal analysis;

References

[1] Pula, R., Khan, F. I., Veitch, B., Amyotte, P. R. A grid based approach for fire and explosion consequence analysis. Process Safety and Environmental Protection, 2006, 84(2): 79-91.

[2] Palazzi, E., Fabiano, B. Analytical modelling of hydrocarbon pool fires: Conservative evaluation of flame temperature and thermal power. Process Safety and Environmental Protection, 2012, 90(2): 121-128.

[3] Elhelw, M., El-Shobaky, A., Attia, A., El-Maghlany, W. M. Advanced dynamic modeling study of fire and smoke of crude oil storage tanks. Process Safety and Environmental Protection, 2020, 146: 670-685.

[4] Ahmadi, O., Mortazavi, S. B., Pasdarshahri, H., Mohabadi, H. A. Consequence analysis of large-scale pool fire in oil storage terminal based on computational fluid dynamic (CFD). Process Safety and Environmental Protection, 2019, 123: 379-389.

[5] Li, Y., Jiang, J., Zhang, Q., Yu, Y., Wang, Z., Liu, H., Shu, C. M. Static and dynamic flame model effects on thermal buckling: Fixed-roof tanks adjacent to an ethanol pool-fire. Process Safety and Environmental Protection, 2019, 127: 23-35.

[6] Palazzi, E., Caviglione, C., Reverberi, A. P., Fabiano, B. A short-cut analytical

model of hydrocarbon pool fire of different geometries, with enhanced view factor evaluation. Process Safety and Environmental Protection, 2017, 110: 89-101.
[7] He, J., Yang, L., Ye, M., Yang, D., Li, A., Huang, L., Zhan, Y. Simulation and application of a detecting rapid response model for the leakage of flammable liquid storage tank. Process Safety and Environmental Protection, 2020, 141: 390-401.
[8] Blinov, V., G. Khudyakov, Diffusion burning of liquids. Army Engineer Research and Development Labs Fort Belvoir VA, 1961.
[9] Zhao, J., Zhang, J., Chen, C., Huang, H., Yang, R. Experimental investigation on the burning behaviors of thin-layer transformer oil on a water layer. Process Safety and Environmental Protection, 2020, 139: 89-97.
[10] Mishra, S., Vishwakarma, P. K., Sharma, A., Mishra, K. B. Experimental investigation of small-scale CS2 (carbon disulphide) pool fires. Process Safety and Environmental Protection, 2021, 145: 203-210.
[11] Kong, D., He, X., Yang, H., Zhang, Z. Experimental study for flame base drag and burning efficiency of spilled crude oil during in-situ burning on water. Process Safety and Environmental Protection, 2019, 131: 48-54.
[12] Gao Z, Wan H, Ji J. The effect of blend ratio on the combustion process of mutually stratified blended fuels pool fire. Proceedings of the Combustion Institute, 2020.
[13] Lin, Y., Hu, L., Zhang, X., Chen, Y. Experimental study of pool fire behaviors with nearby inclined surface under cross flow. Process Safety and Environmental Protection, 2021, 148: 93-103.
[14] Vasanth, S., Tauseef, S. M., Abbasi, T., Abbasi, S. A. CFD simulation of pool fires situated at differing elevation. Process Safety and Environmental Protection, 2015, 94: 89-95.
[15] Deng, L., Tang, F., Ma, X. Experimental study on flame-merging probability and pulsation frequency of annular hydrocarbon pool fires with various inner and outer diameters. Process Safety and Environmental Protection, 2020, 146: 473-480.
[16] Wang, Z., Zhou, K., Zhang, L., Nie, X., Wu, Y., Jiang, J., He, L. Flame Extension Area and Temperature Profile of Horizontal Jet Fire Impinging on a Vertical Plate. Process Safety and Environmental Protection, 2021, 147: 547-558.
[17]. Zukoski, E.E., T. Kubota, B. Cetegen, Entrainment in fire plumes. Fire Safety Journal, 1981, 3(3): 107-121.
[18] Hiroshi, K., Taro, Y. Air entrainment and thermal radiation from heptane pool fires. Fire Technology, 1988, 24(1): 33-47.
[19] Loy, Y. Y., Rangaiah, G. P., Lakshminarayanan, S. Surrogate modelling of net radiation flux from pool fires in a hydrocarbon storage facility. Process Safety and Environmental Protection, 2018, 114: 296-309.
[20] Rew, P. J., Hulbert, W. G., Deaves, D. M. Modelling of thermal radiation from external hydrocarbon pool fires. Process safety and environmental protection, 1997, 75(2): 81-89.
[21] Ramsden, N., Abusaieda, K. A. A study of water cooling using different water application techniques to protect storage tank walls against thermal radiation. Process Safety and Environmental Protection, 2017, 109: 577-598.
[22] Ji J, Ge F, Qiu T. Experimental and theoretical research on flame emissivity and

radiative heat flux from heptane pool fires. Proceedings of the Combustion Institute, 2020.
[23] Ge F, Simeoni A, Ji J, et al. Experimental study on the evolution of heat feedback in multiple pool fires. Proceedings of the Combustion Institute, 2020.
[24] Wan H, Yu L, Ji J. Experimental study on mass burning rate and heat feedback mechanism of pair of unequal circular pool fires of heptane. Proceedings of the Combustion Institute, 2020.
[25] Sharma, A., Mishra, K. B. Experimental set-up to measure the maximum mass burning rate of storage tank fires. Process Safety and Environmental Protection, 2019, 131: 282-291.
[26] Farahani, H. F., Shi, X., Simeoni, A., Rangwala, A. S. A study on burning of crude oil in ice cavities. Proceedings of the Combustion Institute, 2015, 35(3): 2699-2706.
[27] Bellino, P. W., A. S. Rangwala, M. R. Flynn, A study of in situ burning of crude oil in an ice channel. Proceedings of the Combustion Institute, 2013, 34(2): 2539-2546.
[28] Smith, B., Wong, C. A., Boyko, E. J., Phillips, C. J., Gackstetter, G. D., Ryan, M. A., The effects of exposure to documented open-air burn pits on respiratory health among deployers of the Millennium Cohort Study. Journal of occupational and environmental medicine, 2012, 54(6): 708-716.
[29] Magnus, G. Tests on combustion velocity of liquid fuels and temperature distribution in flames and beneath surface of the burning liquid. in Proc. 1st Int. Symp. on the Use of Models in Fire Research. 1961.
[30] Dlugogorski, B., M. Wilson, Effect of Ullage on Properties of Small-Scale Pool Fires. Developments in Chemical Engineering and Mineral Processing, 2000, 8(12): 149-166.
[31] Hu, L., J. Hu, J. L. de Ris, Flame necking-in and instability characterization in small and medium pool fires with different lip heights. Combustion and Flame, 2015, 162(4): 1095-1103.
[32] Shi, X., Sahu, A. K., Nair, S., Raghavan, V., Rangwala, A. S. Effect of ullage on burning behavior of small-scale pool fires in a cavity. Proceedings of the Combustion Institute, 2017, 36(2): 3113-3120.
[33] Kuang, C., Hu, L., Zhang, X., Lin, Y., Kostiuk, L. W. An experimental study on the burning rates of n-heptane pool fires with various lip heights in cross flow. Combustion and Flame, 2019, 201: 93-103.
[34] Liu C, Ding L, Jangi M, et al. Experimental study of the effect of ullage height on flame characteristics of pool fires. Combustion and Flame, 2020, 216: 245-255.
[35] Liu C, Ding L, Ji J. Experimental study of the effects of ullage height on fire plume centerline temperature with a new virtual origin model. Process Safety and Environmental Protection, 2021, 146: 961-967.
[36] Ma, L., Nmira, F., Consalvi, J. L. Large Eddy Simulation of medium-scale methanol pool fires-effects of pool boundary conditions. Combustion and Flame, 2020, 222: 336-354.
[37] Ji J, Wang C, Yu L. Physical models of flame height and air entrainment of two adjacent buoyant turbulent jet non-premixed flames with different heat release rates. Proceedings of the Combustion Institute, 2020.

[38] Wan H, Gao Z, Ji J, et al. Experimental study on merging behaviors of two identical buoyant diffusion flames under an unconfined ceiling with varying heights. Proceedings of the Combustion Institute, 2019, 37(3): 3899-3907.
[39] Liu C, Wan H, Ji J, et al. Flame spread characteristics and a multi-cylinder radiation model for diesel tray fires against a sidewall. International Journal of Thermal Sciences, 2019, 139: 433-439.
[40] McGrattan, K., Hostikka, S., Floyd, J., Vanella M. Fire Dynamics Simulator User's Guide, National Institute of Standards and Technology, Gaithersburg, Maryland, 2019.
[41] Oliveira, R. L. F., Doubek, G., Vianna, S. S. On the behaviour of the temperature field around pool fires in controlled experiment and numerical modelling. Process Safety and Environmental Protection, 2019, 123: 358-369.
[42] Yu, L. X., Beji, T., Maragkos, G., Liu, F., Weng, M. C., Merci, B. Assessment of numerical simulation capabilities of the fire dynamics simulator (FDS 6) for planar air curtain flows. Fire Technology, 2018, 54(3): 583-612.
[43] Chiu, C. W., Li, Y. H. Full-scale experimental and numerical analysis of water mist system for sheltered fire sources in wind generator compartment. Process Safety and Environmental Protection, 2015, 98: 40-49.
[44] Wen, J. X., Kang, K., Donchev, T., Karwatzki, J. M. Validation of FDS for the prediction of medium-scale pool fires. Fire Safety Journal, 2007, 42(2): 127-138.
[45] McGrattan, K., McDermott, R., Hostikka, S., Floyd, J., Vanella, M., Fire dynamics simulator technical reference guide, Volume 1: Mathematical Model, National Institute of Standards and Technology, Gaithersburg, Maryland, 2018.
[46] Mcdermott Randall, Mcgrattan Kevin B., Floyd Jason. A simple reaction time scale for under-resolved fire dynamics. Fire Safety Science, 2011, 10: 809-820.
[47] Grosshandler, W. L. RADCAL: a Narrow-band Model for Radiation. Calculations in a Combustion Environment, NIST Technical Note, 1993, 1402.
[48] Eng, T., PyroSim User Manual. The RJA Group Inc, Chicago, USA, 2011.
[49] K. B. McGrattan, H.R. Baum, R.G. Rehm, Large eddy simulations of smoke movement, Fire Safety Journal, 1998, 30: 161-178.
[50] W. Malalasekera, H.K. Versteeg, K. Gilchrist, A review of research and an experimental study on the pulsation of buoyant diffusion flames and pool fires, Fire and Material, 1996, 20: 261-271.
[51] Wang, H., Wang, E., Li, Z., Shen, R., Liu, X., Gao, X., Zhang, Q. Study on safety pressure of water jet breaking coal based on the characteristic analysis of electromagnetic radiation signal. Process Safety and Environmental Protection, 2020, 144: 284-296.
[52] Cheung, S. C. P., Yeoh, G. H., Cheung, A. L. K., Yuen, R. K. K., Lo, S. M. Flickering behavior of turbulent buoyant fires using large-eddy simulation. Numerical Heat Transfer, Part A: Applications, 2007, 52(8): 679-712.
[53] Le Maoult, Y., Sentenac, T., Orteu, J. J., Arcens, J. P. Fire detection: a new approach based on a low cost CCD camera in the near infrared. Process Safety and Environmental Protection, 2007, 85(3): 193-206.
[54] Ahmadi, O., Mortazavi, S. B., Pasdarshahri, H., Mahabadi, H. A., Sarvestani, K. Modeling of boilover phenomenon consequences: Computational fluid dynamics (CFD)

and empirical correlations. Process Safety and Environmental Protection, 2019, 129: 25-39.
[55] Lin, K. C., Faeth, G. M., Sunderland, P. B., Urban, D. L., Yuan, Z. G. Shapes of non-buoyant round luminous hydrocarbon/air laminar jet diffusion flames. Combustion and Flame, 1999, 116(3): 415-431.
[56] Tieszen, S. R., Nicolette, V. F., Gritzo, L. A., Holen, J. K., Murray, D., Moya, J. L. Vortical structures in pool fires: Observation, speculation, and simulation. Sandia National Laboratories Report, SAND96-2607, 1996.
[57] Cheung, S.C.P. G.H. Yeoh, A fully-coupled simulation of vortical structures in a large-scale buoyant pool fire. International Journal of Thermal Sciences, 2009, 48(12): 2187-2202.
[58] Smith R. K., Morton B. R., Leslie L. M. The role of dynamic pressure in generating fire wind. Journal of Fluid Mechanics, 1975, 68(1): 1-19.
[59] Charland A. M., Clements C. B. Kinematic structure of a wildland fire plume observed by Doppler lidar. Journal of Geophysical Research: Atmospheres, 2013, 118(8): 3200-3212.
[60] Samiran, N. A., Ng, J. H., Jaafar, M. N. M., Valera-Medina, A., Chong, C. T. Swirl stability and emission characteristics of CO-enriched syngas/air flame in a premixed swirl burner. Process Safety and Environmental Protection, 2017, 112: 315-326.
[61] Chong, C. T., Ng, J. H., Aris, M. S., Mong, G. R., Shahril, N., Ting, S. T., Zulkifli, M. F. Impact of gas composition variations on flame blowout and spectroscopic characteristics of lean premixed swirl flames. Process Safety and Environmental Protection, 2019, 128: 1-13.
[62] Jangi, M. B.Z. Dlugogorski, On wall fire interaction in a small pool fire: A large-eddy simulation study. Fire Safety Journal, 2017, 92: 199-209.
[63] Jangi, M., M. Altarawneh, B.Z. Dlugogorski, Large-eddy simulation of methanol pool fires using an accelerated stochastic fields method. Combustion and Flame, 2016, 173: 89-98.
[64]. Brookes S J, Moss J B. Measurements of soot production and thermal radiation from confined turbulent jet diffusion flames of methane. Combustion and Flame, 1999, 116(1-2): 49-61.
[65]. Lopez-Parra F, Turan A. Computational study on the effect of turbulence intensity and pulse frequency in soot concentration in an acetylene diffusion flame//International Conference on Computational Science. Springer, Berlin, Heidelberg, 2005: 120-128.